

(21) Utilizing the National Corn-to-Ethanol Pilot Plant to Develop a Predictive Model for Distillers Dried Grain for the Fuel Ethanol and Animal Feed Industries

The objective of this two-year effort is to develop and validate a neural network predictive plant model for the composition of Distillers Dried Grain with Solubles (DDGS), a coproduct resulting from the dry grind fuel ethanol process.

Total project cost: \$807,221

Funding request: \$633,149

Project Lead: Southern Illinois University Edwardsville: National Corn-to Ethanol Research Center

Project Participants: Washington University, St. Louis, Missouri-Department of Chemical Engineering; Emerson Process Management; Illinois Department of Commerce and Economic Opportunity.

Start Date: May 23, 2005

End Date: May 23, 2007

Presentations/Publications

Brian Wrenn gave a talk on February 20, 2007 at the National Ethanol Conference in Tucson, AZ that described preliminary results from this project.

Patents

None.

Progress in Past Quarter and Current Status

5.1.1. Experimental Design

The NCERC performed two pilot-plant experiments investigate the effects of liquefaction, saccharification, and solids-processing conditions on fermentation and DDGS quality. The purpose of these experiments was to determine how changes in plant operating conditions affect the rate and yield of fermentation and the quality of the DDGS coproduct. The experimental design is shown in Table 1. Ten operational factors were tested at two levels in these experiments; nine of those factors were also tested at a third (midpoint) level. Other plant conditions were consistent in all treatment conditions (a.k.a., "runs"). The consistent conditions are shown in Table 2. Each treatment condition was maintained long enough to completely fill a single fermenter (about 20 hrs). Slurry, mash, and beer samples were collected at approximately eight-hour intervals. The solids concentration and dextrose equivalents (DE) value were measured in slurry and wort samples, soluble carbohydrates (e.g., glucose and oligoaccharides) and ethanol were measured in beer samples, and several characteristics related to the nutritional value will be measured in DDGS samples. The soluble carbohydrate and ethanol concentrations were used to estimate fermentation kinetic parameters.

5.1.2. Experimental Results

The effects of each experimental factor shown in Table 1 on several fermentation parameters were determined multiple linear regression using the tool available in Systat (SPSS Science, Inc.). Several treatments (runs 1, 10, 11, and 12) were independently

replicated, and the results of the replicates were included as independent data in the regression analysis. Since only the slurry-system parameters could affect the slurry-tank DE, these data were analyzed using standard factor analysis methods, which can also consider interactions among treatment factors. Since five slurry-system treatment factors were investigated, which requires 32 runs to evaluate all possible

Table 1: Experimental conditions for pilot-plant experiments*

Run	mill screen size (in)	process water flow (lbs/min)	target solids conc. (%)	slurry tank temp (°F)	slurry tank level (%)	slurry tank enzyme flow (g/hr)	jet cooker temp (°F)	mash tank temp (°F)	mash tank level (%)	mash tank enzyme flow (g/hr)
1	4/16	15.1	32	182	90	95	225	181	85	190
2	4/16	18.1	28	195	60	95	235	192	85	150
3	4/16	16.6	30	188.5	75	85	230	186.5	75	170
4	4/16	15.1	32	195	90	95	225	192	65	190
5	4/16	18.1	28	182	60	95	235	181	65	150
6	4/16	15.1	32	195	60	75	235	181	85	190
7	4/16	18.1	28	182	90	75	225	192	85	150
8	4/16	15.1	32	182	60	75	235	192	65	190
9	4/16	18.1	28	195	90	75	225	181	65	150
10	7/16	15.1	32	182	90	75	235	192	65	150
11	7/16	18.1	28	195	60	75	225	181	65	190
12	7/16	15.1	32	195	90	75	235	181	85	150
13	7/16	18.1	28	182	60	75	225	192	85	190
14	7/16	16.6	32	188.5	75	85	230	186.5	75	170
15	7/16	15.1	30	195	60	95	225	192	65	150
16	7/16	18.1	28	182	90	95	235	181	65	190
17	7/16	15.1	32	182	60	95	225	181	85	150
18	7/64	18.1	28	195	90	95	235	192	85	190

*the first pilot-plant experiment (Oct. '06) included runs 1-9 and the second pilot-plant experiment (Jan. '07) including runs 10-18; consistent conditions were as described in text

Table 2: Consistent conditions for pilot-plant experiments*

Condition	Set point
corn feed rate	510 lbs/hr
process water temperature	200 °F

jet cooker flow rate	3 gal/min
second mash tank (TA-1030) level	75%
third mash tank (TA-1220) level	75%
fermenter volume	3600 gals
fermenter temperature	90 °F

combinations of treatment factors at two levels, and only 16 runs were conducted at those levels, some of the two-factor and all of the three-factor interactions are confounded. Because of the large variability in the slurry-tank DE measurements (probably due to nonrepresentative sampling), none of the main effects were significant. Hammer-mill screen size was significant at the 90% confidence level ($P = 0.099$), however, and as expected, it exerted a negative effect on slurry DE. This was expected because the starch should be extracted from larger particles more slowly than from small particles. The interaction between slurry tank level and temperature was significant at the 95% confidence level. This two-factor interaction was also negative, suggesting that at the higher temperature, increasing the tank residence time had a smaller-than-expected effect on DE. This suggests that the amylase enzyme might have been inactivated at the high slurry-tank temperature (195 °F); so, the hydrolysis rate was lower than at the lower temperature. The effect of temperature was not sufficient to result in a significant main effect, however.

Wort samples were collected from the first (TA-950) and third (TA-1220) mash tanks. As expected, the DE increased with time in the system. The average DE (over all experimental conditions) for samples collected from the slurry tank (TA-990) and the two mash tanks are shown in Table 3. Mash-tank DE data were more reproducible, as is shown by the standard errors of the mean (SEM) for each sample location in Table 3, suggesting that it was easier to collect representative samples downstream in the process. The SEM were based on independent replicates of identical treatments, whereas the standard deviations (SD) shown for the average DE at each sample location also included contributions from varying experimental conditions. Since the SEM for independent replicates of slurry tank samples was almost equal to the SD over all experimental conditions, it is not surprising that significant main effects could not be identified at that location.

Table 3: Dextrose equivalents (DE) in samples from the slurry and mash tanks

sample location	DE \pm SD	SEM*
slurry tank (TA-990)	10.6 \pm 2.6	2.1
first mash tank (TA-950)	12.0 \pm 2.0	0.9
third mash tank (TA-1220)	14.4 \pm 2.0	0.6

*SEM = standard error of the mean for independent replicates of identical treatments

The effects of treatment factors on DE in samples collected from both mash-tank locations are shown in Tables 4 and 5, which report the magnitude of each treatment effect along with the standard error and the probability that the effect is equal to zero

(i.e., P values less than 0.05 are significantly different from zero at the 95% confidence interval). The mash tank temperature exerts a negative effect at both locations, suggesting that the enzyme might be inactivated at the higher temperature (192 °F) used in these experiments. The effect was significant at the 95% confidence level in samples collected from the third mash tank, where the enzyme was exposed to the higher temperature for a longer period of time, but it was only slightly less significant in the first mash tank. The effect of the hammer-mill screen diameter was positive at both locations, which is somewhat surprising because (as described above) one would expect the starch to be extracted more easily from small particles than from large ones. The slurry-tank temperature and jet-cooker temperature both exerted negative effects in the first mash tank but were not important in the third mash tank. This suggests that those effects are transient, and therefore, should not affect fermentation kinetics. The rate of enzyme input to the mash tank exerted a statistically significant positive effect on DE in samples collected from the third mash tank but not the first mash tank. The relationship between the observed and predicted DE values are shown in Figures 1 (TA-950) and 2 (TA-1220).

Table 4: Factor main effects on wort DE in samples collected from the first mash tank (TA-950)

factor	effect \pm SE*	P**
constant	80.7 \pm 22.3	0.002
hammer-mill screen diameter	48.1 \pm 14.5	0.004
slurry-tank temperature	-0.115 \pm 0.055	0.051
mash-tank temperature	-0.125 \pm 0.065	0.070
jet-cooker temperature	-0.121 \pm 0.071	0.107

*SE = standard error of factor effect (computed from regression statistics)

**P = probability that effect is zero

Table 5: Factor main effects on wort DE in samples collected from the third mash tank (TA-1220)

factor	effect \pm SE*	P**
constant	57.8 \pm 10.5	0.0004
mash-tank temperature	-0.253 \pm 0.051	0.0001
mash-tank enzyme input rate	0.041 \pm 0.014	0.010
hammer-mill screen diameter	21.1 \pm 11.4	0.081
process-water flow rate	-0.298 \pm 0.187	0.129

*SE = standard error of factor effect (computed from regression statistics)

**P = probability that effect is zero

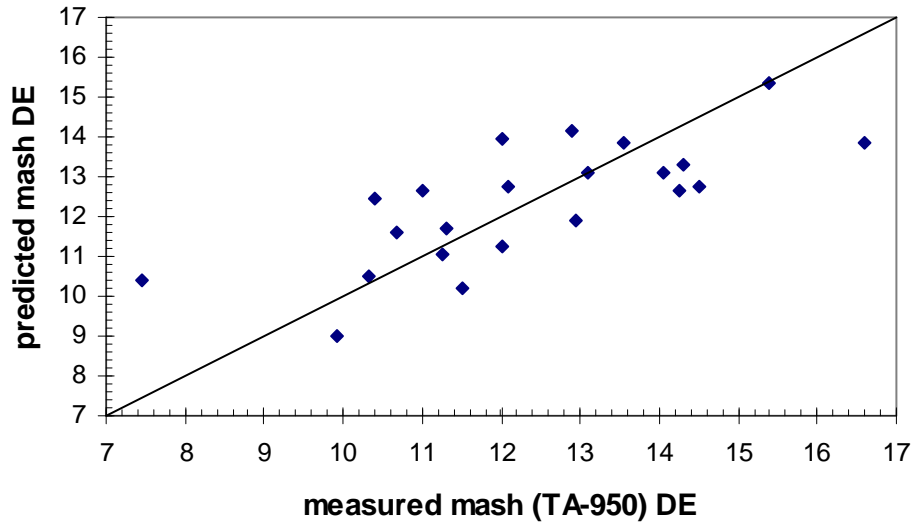


Figure 1: Fit of multiple-regression model to the observed DE in sample collected from the first mash tank (TA-950). DE was predicted for each sample based on the experimental conditions using the parameters given in Table 4. The correlation coefficient (r^2) for the multiple regression model was 0.538.

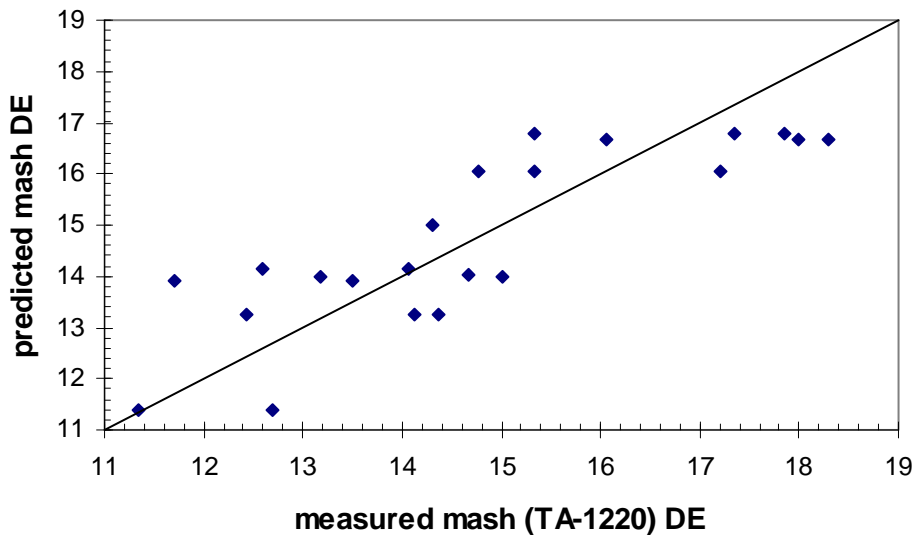


Figure 2: Fit of multiple-regression model to the observed DE in samples collected from the third mash tank (TA-1220). DE was predicted for each sample based on the experimental conditions using the parameters given in Table 5. The correlation coefficient (r^2) for the multiple-regression model was 0.702.

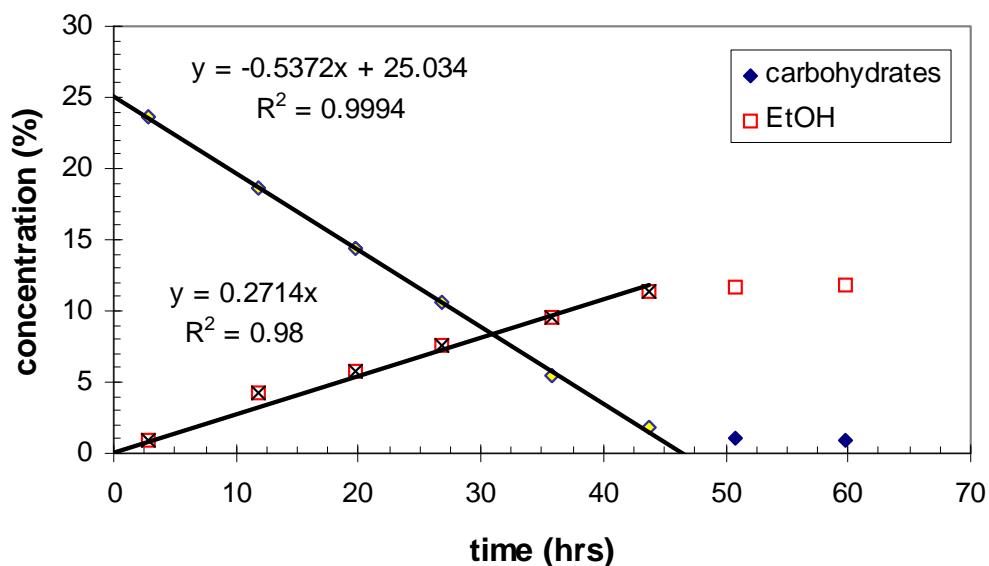


Figure 3: Kinetics of carbohydrate consumption and ethanol production in a fermenter filled with wort prepared using the conditions for Run 1 (Table 1). The equations shown represent the best fits of zero-order kinetics models to the experimental results.

The upstream process conditions that affect fermentation kinetics were identified by measuring carbohydrate consumption and ethanol production kinetics. The carbohydrate concentrations were expressed as glucose equivalents by calculating the glucose equivalent mass concentration for each oligosaccharide that was measured. The conversion factors for maltose (DP2), maltotriose (DP3), and larger soluble oligosaccharides (DP \geq 4) were 1.05 g glucose/g DP2, 1.07 g glucose/g DP3, and 1.09 g glucose/g DP \geq 4, respectively. The kinetics for a typical fermenter are shown in Figure 3. The rates of carbohydrate consumption and ethanol production were estimated by linear regression because a simple zero-order model for a batch reactor was the simplest model that explained the data well.

The upstream process conditions that affected fermentation kinetics most strongly are identified in Tables 6 and 7 for carbohydrate consumption and ethanol production, respectively. The rate of carbohydrate consumption was positively affected by process water flow rate and slurry-tank level and negatively affected by the slurry-tank temperature. Surprisingly, none of these factors exerted a significant effect on the rate of ethanol production. Instead, the rate of ethanol production was stimulated by the mash-tank temperature and inhibited by the hammer-mill screen size, the jet-cooker temperature, and the mash-tank level, respectively. The fit of these multiple regression models to the fermentation kinetics data is shown in Figures 4 and 5 for carbohydrate consumption and ethanol production, respectively.

Table 6: Factor main effects on carbohydrate consumption rate in fermenters

factor	effect \pm SE*	P**
constant	0.88 \pm 0.35	0.024
process-water flow rate	0.028 \pm 0.008	0.002
slurry-tank temperature	-0.0044 \pm 0.0018	0.024
slurry-tank level	0.0014 \pm 0.0008	0.091

*SE = standard error of factor effect (computed from regression statistics)

**P = probability that effect is zero

Table 7: Factor main effects ethanol production rate in fermenters

factor	effect \pm SE*	P**
constant	0.40 \pm 0.18	0.040
mash-tank temperature	0.0013 \pm 0.0006	0.039
hammer-mill screen diameter	-0.27 \pm 0.13	0.059
jet-cooker temperature	-0.0013 \pm 0.0006	0.068
mash-tank level	-0.0005 \pm 0.0003	0.119

*SE = standard error of factor effect (computed from regression statistics)

**P = probability that effect is zero

6. Plans for the following quarters

All pilot-plant experiments have been completed. Samples that were collected during the two most-recent pilot-plant experiments are being analyzed. In addition, plant operational data from the last two experiments are being compiled. These operations data will support the statistical analysis of fermentation performance and DDGS quality data. They will also be used to create a neural-network model that relates plant operational data to DDGS quality. In addition, we are developing a model of the NCERC's drum dryer based on mass and energy balances that can be used to optimize dryer performance. This combination of fundamental analysis based on physical and chemical principles with empirical analysis based on observations made during plant operations will allow us to provide practical guidance on optimization of dryer performance to balance the competing demands of obtaining low DDGS moisture and high nutritional quality.

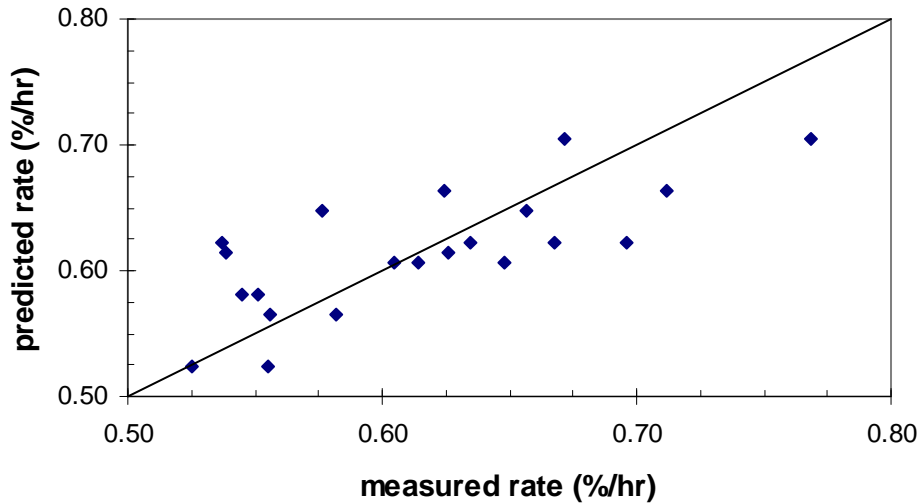


Figure 4: Fit of multiple-regression model to the carbohydrate consumption rate data measured in fermenters. The rate of carbohydrate consumption was predicted based on the experimental conditions using the parameters given in Table 6. The correlation coefficient (r^2) for the multiple-regression model was 0.539.

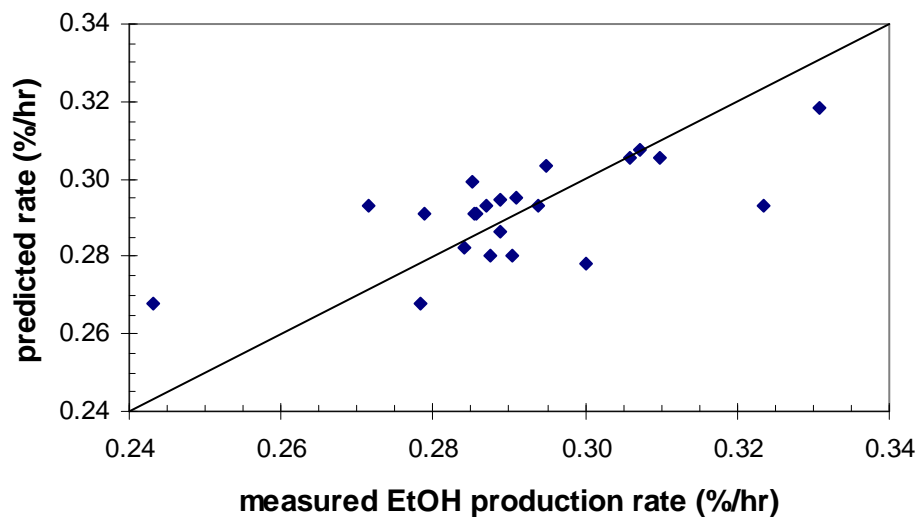


Figure 5: Fit of multiple-regression model to the ethanol production rate data measured in fermenters. The rate of carbohydrate consumption was predicted based on the experimental conditions using the parameters given in Table 7. The correlation coefficient (r^2) for the multiple-regression model was 0.482.

(22) Iron-Based Mixed Metal Carbide Fischer-Tropsch Catalysts

This three-year effort will seek to develop a more active, selective, attrition resistant and stable Fe FTS catalysts based on formulations containing a second metal (besides Cu) capable of forming mixed metal carbides with Fe.

Total project cost: \$1,334,594
 Funding request: \$875,499
 Project Lead: Clemson University
 Project Participants: Louisiana State University; RTI; Rentech; Sud-Chemie, Inc.; South Carolina Energy Office; Louisiana State Energy Office

Start Date: August 31, 2005
 End Date: August 31, 2008

Presentations/Publications

None.

Patents

None.

Progress in Past Quarter and Current Status:

Project activities are progressing in accordance with the project schedule (Table 1). During this 6th quarter of activities the main focus has been on catalyst characterization of catalysts containing different transition metals. These activities are described in the following section comprising the experimental methodology and results.

Table 1: Project Schedule

Tasks	Activity											
	Year 1				Year 2				Year 3			
	1	2	3	4	1	2	3	4	1	2	3	4
Task 1: Catalyst Prep.	X	X	X		X		X		X		X	
Task 2: Catalyst Charac.	X	X	X	X	X	X	X	X	X	X	X	
Task 3: Reaction Study		X	X	X	X	X	X	X	X	X	X	X
Task 4: Slurry Phase Reactor Testing			X	X			X	X		X	X	
Task 5: Eval. of Comm. Potential					X				X			X

1.1 Methodology

1.1.1 Catalyst Preparation

Catalysts are prepared according to the general formulation: 100-x)Fe/xMe/5Cu/17Si, where *Me* indicates a third-metal, and x is the mol% using the constant pH precipitation technique [1,2]. Fe(NO₃)₃·9H₂O and CuN₂O₆·3H₂O are added together into 60 ml of water while tetraethylorthosilicate (Si(OC₂H₅)₄, TEOS) is added into 40 ml of propanol. These 2 solutions are mixed and then *Me* is added into the final solution. The resulting solution is heated to 83 ± 3°C. Aqueous NH₄OH (~2.7 M) preheated to 83 ± 3°C is slowly added into the solution containing Fe, Cu, Si and *Me* precursors under vigorous and continuing stirring for 3 min. The resulting pH after

formation of a precipitate is 8-9. The precipitate is aged in a vessel at room temperature for 17-18 h and then thoroughly washed with deionized water to remove excess NH_3 until the pH is 7-8 (1.3-1.5 liters of deionized water used). The washed precipitate is dried in an oven for 18-24 h at 120°C to remove excess water. After drying, the catalyst precursor is calcined in static air at 300°C for 5 h, then cooled to room temperature over a 2-h period in a muffle furnace. The fresh calcined catalyst is sieved $< 90 \mu\text{m}$ before reaction testing and other characterizations.

1.1.2 Catalyst Characterization

Catalysts are characterized by elemental analysis, N_2 adsorption (BET, pore volume, pore size distribution), XRD (Fe and *Me* crystalline phases formed), CO pulse chemisorption (surface metal atoms), SEM (the morphologies of catalyst), EDX (the elemental distribution and concentration), TPR (reducibility of Fe) and EXAFS (the structure and coordination of atoms).

a) Elemental Analysis

Elemental analysis is performed to determine the composition of elements in the bulk of catalysts. The composition content of catalysts is determined using ICP-OES at Galbraith Laboratories.

b) N_2 Adsorption

The BET surface area, pore volume, average pore diameter, and pore size distribution of the catalysts are determined by N_2 physisorption using a Micromeritics ASAP 2010 automated system. A 0.3 g catalyst sample is degassed in the Micromeritics ASAP 2010 at 100°C for 1 h and then at 300°C for 2 h with $10^\circ\text{C}/\text{min}$ ramping rate prior to analysis. The analysis is done using N_2 adsorption at -196°C .

c) X-Ray Diffraction (XRD)

XRD is used to determine the phase composition of Fe catalysts as prepared and after pretreatments. The XRD spectrum of the catalysts is collected using an X-ray diffractometer, Scintag 2000 x-ray diffractometer, using monochromatized Cu K_α radiation (40 kV, 40 mA) and a Ge detector using a step scan mode at a scan rate of 0.02° (2θ) per second from 10 - 80° . XRD peak identification is done by comparison to the JCPDS database software.

d) CO-Pulse Chemisorption

Fe dispersion is determined by pulsing CO over the reduced catalyst. Approximately 0.2 g of catalyst is put in a quartz tube, incorporated in a temperature-controlled oven and connected to a thermal conductivity detector (TCD). He is used as a carrier gas for this system. Prior to chemisorption, the catalyst is reduced in a flow of hydrogen (50 cc/min) at 280°C for 12 h. Afterwards, the sample is cooled down to 35°C with He 30cc/min. CO is pulsed at 35°C over the reduced catalyst until the TCD signal is constant. An

assumed stoichiometry ratio on the surface of $\text{CO}:\text{Fe}_s^0 = 1:2$ is used [3].

e) Extended X-ray absorption fine structure (EXAFS)

EXAFS is used to provide information on the structure and coordination of atoms on the catalyst surface. The catalysts are studied at the Center for Advanced Microstructures and Devices (CAMD) at LSU.

f) Scanning Electron Microscopy (SEM) and Energy Dispersive X-Ray Spectroscopy (EDX)

The morphologies of the catalyst samples and the elemental concentration on the catalyst surface as well as elemental distributions are studied using SEM and EDX, respectively. SEM and EDX are performed using a Hitachi FESEM-S4800 under the backscattering electron (BSE) and scanning electron (SE) mode. The accelerating voltage was 20 kV with a working distance of 15 mm.

g) Temperature program reduction of H_2 (TPR)

TPR is performed to test reducibility of Fe using Altamira AMI-1 system. A fresh calcined catalyst (0.2 g) is first heated to 200°C ($10^\circ\text{C}/\text{min}$) under 30 cc/min of He and held for 2 h before it is cooled down to 35°C . Then the reducibility of catalyst is tested using 5% H_2/Ar (30cc/min) by increasing the temperature up to 700°C with $5^\circ\text{C}/\text{min}$ heating rate. A thermal conductivity detector (TCD) is used to measure H_2 consumption and it is calibrated by reduction of Ag_2O . The reducibility of Fe is calculated based on 100% reducibility of Fe_2O_3 to Fe.

1.1.3 CO Hydrogenation Reaction Studies

CO hydrogenation is performed using 0.1 g of catalyst packed in a fixed bed-quartz reactor with i.d. = 8 mm. The total flow rate used is 60 cc/min with the H_2/CO ratio of 2/1 in a balance of He. The catalyst sample is pretreated in 30 cc/min of H_2 at 280°C for 12 h with $2^\circ\text{C}/\text{min}$ ramping rate prior to CO hydrogenation.

CO hydrogenation reactions are carried out at 280°C and at 1.8 atm. The product streams are analyzed by gas chromatography.

1.2 Results and Discussion

During this quarter, we have done SEM, EDX and TPR for catalyst characterization of the catalysts with 5 mol% of added metal prepared and reported previously. For a comparison purpose, summarized results of the catalyst activity with and without second metal addition for CO hydrogenation and water-gas shift (WGS) reaction from previous report are shown in Figures 1 and 2,

respectively. FeCr and FeMn are the best 2 catalysts showing the highest catalyst activity for both CO hydrogenation and WGS reaction. Adding Mo, Ta and V to the Fe-based catalysts also enhanced the catalyst activity but in lesser degrees while an Fe-based catalyst with added W showed less active than the benchmark catalyst.

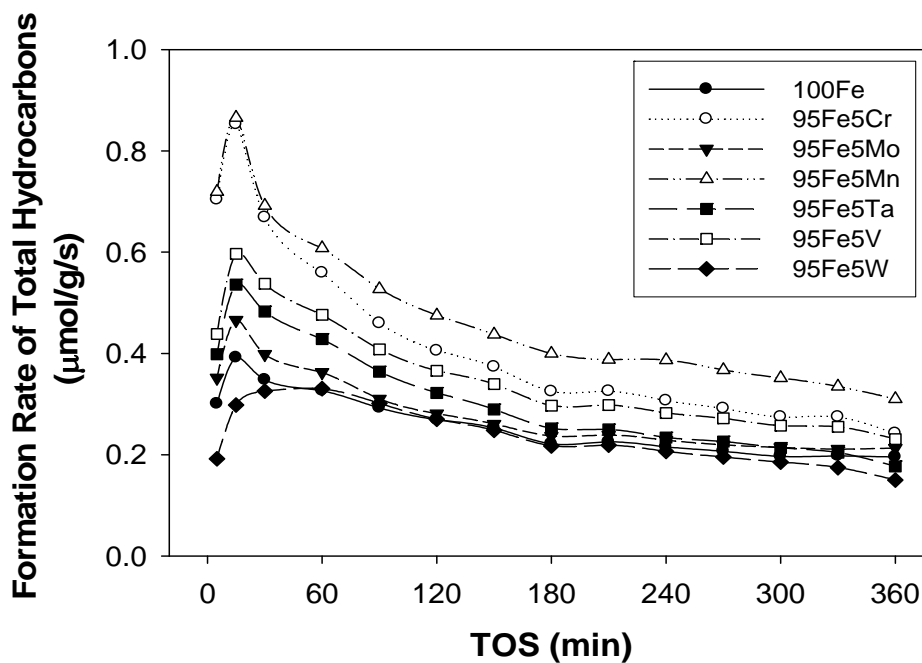


Figure 1: Formation rate of total hydrocarbon (C_1-C_8) at 280°C with the addition of various transition metals.

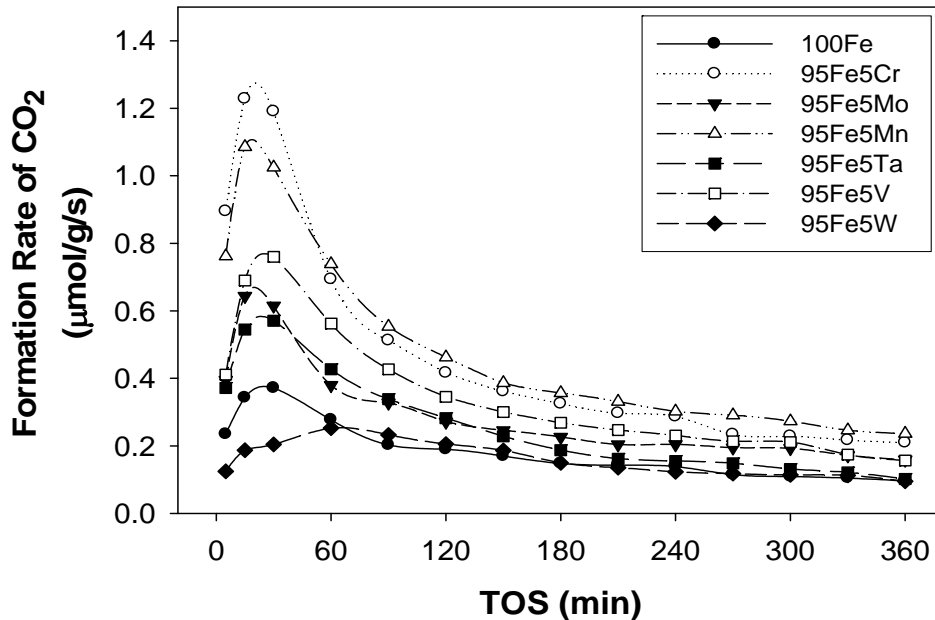


Figure 2:

Formation rate of CO₂ at 280°C with the addition of various transition metals.

TPR peak temperature and %reducibility of Fe are shown in Figure 3 and Table 2. %Reducibility of Fe for samples containing various transition metals is calculated based on 100% Fe₂O₃ standard reduced to Fe and the results show that %reducibility of Fe varied in the range of 83-98%. The addition of the third transition metal (besides Cu which is the 2nd) at 5 mol% did not significantly affect the peak temperature (287-295°C) with the exception of the FeV catalyst. The reducibility of Fe is delayed by the addition of V showing a peak temperature shift of about 30°C respect that of the 100Fe catalyst. However, the presence of V did not show any impact on the amount of Fe reduced. It has been suggested that V can distribute in the Fe oxide structure without interfering with the dispersion of Fe resulting in a relatively normal amount of H₂ uptake [4].

Figure 3:

TPR profiles of the fresh calcined Fe-based catalysts.

TPR profiles of the fresh calcined Fe-based catalysts.

Table
Fe-

Catalyst ^a	TPR peak temperature ^b (°C)	%Reducibility ^c
100Fe	288	92
95Fe/5Cr	273	98
95Fe/5Mo	294	84
95Fe/5Mn	295	88
95Fe/5Ta	288	83
95Fe/5V	324	96
95Fe/5W	292	85

2: TPR results of based mixed metal catalysts.

^a Containing 5Cu and 17Si.

^b Max error = ± 3%.

^c Based on a 100% reducibility of Fe₂O₃ standard to Fe with max error = ± 3%.

Although the FeV catalyst exhibited a relatively high amount of Fe reduced, the reduction was completed at 320°C which is higher than the pretreatment temperature of 280°C. Therefore, the reduction of Fe would have been less at around 280°C. In addition, lower %reducibilities of Fe was found for the W, Mo and Ta added catalyst (83-85%) for which lower catalyst activity was observed (Figures 1 and 2). This suggests that metallic Fe is required for the catalyst to carry out the reaction. However, not only reducibility of Fe but also the BET surface area affects the activity of catalyst. As can be seen for FeMn catalyst, %reducibility of Fe of the FeMn catalyst was not as high as that of the unpromoted Fe-based

catalyst, but its BET surface area was very high (373 m²/g), as shown in Table 3. On the other hand, the activity of the FeW catalyst was the least and its BET surface area was only 295 m²/g.

Table 3: The BET surface area, pore volume and pore size of Fe-based catalysts.

Catalyst ^a	Max Rate ^b ($\mu\text{mol/g/s}$)	BET S.A. (m^2/g)	Pore volume (cm^3/g)	Pore size (A)
95Fe/5Cr	1.98	351	0.29	33
95Fe/5Mn	1.51	373	0.32	34
95Fe/5V	1.26	338	0.26	30
95Fe/5Ta	1.09	341	0.29	34
95Fe/5Mo	1.10	342	0.27	32
95Fe/5W	0.48	295	0.25	34
100Fe	0.74	329	0.34	42

^a with 5Cu/17SiO₂

^b total rate of hydrocarbon and CO₂ production

The morphologies of the catalyst samples were studied using SEM. SEM micrographs are shown in Figure 4. There was no appreciable difference among the catalysts with third metals and the benchmark catalyst. The catalyst particles were observed to be flat and irregular shaped with some uneven surfaces. Due to the similarity of SEM micrographs for the catalysts studied (100Fe, FeMn and FeW), SEM was not performed for the rest of the catalysts (FeTa, FeMo, FeV, FeZr and FeCr).

Figures removed—too large to upload with report

Figure 4: SEM micrographs of fresh calcined (a) 100Fe/5Cu/17SiO₂, (b) 95Fe/5Mn/5Cu/17SiO₂, and (c) 95Fe/5W/5Cu/17SiO₂ catalysts.

The elemental distribution on the cross-section of fresh calcined 100Fe catalyst was observed by EDX mapping. As shown in Figure 5, all elements were well distributed. This is also true for the catalyst with added Mn (Figure 6), indicating that all elements in the catalysts were well throughout the catalysts.

Figures removed—too large to upload with report

Figure 5: SEM micrograph and EDX mapping of a fresh calcined 100Fe/5Cu/17SiO₂ granule.

Figures removed—too large to upload with report

Figure 6: SEM micrograph and EDX mapping of a fresh calcined 95Fe/5Mn/5Cu/17SiO₂ granule.

At LSU, XRD was performed to determine the Fe phase of the tungsten containing samples using Fe K_α excitation. The tuned synchrotron radiation (Fe K_α) in conjunction with noise-free Si-based sample holders was able to improve the signal to noise ratio. Figure 7 shows that data obtained using the Fe K_α excitation is superior to that obtained using Cu K_α excitation. Initial data analysis shows the peaks correspond to a carbide and oxide phase.

Figure removed—to large to upload with report

Figure 7: XRD comparison using Cu K_α (left) and Fe K_α excitation (right)

The EXAFS Company is currently repairing the Lytle Detector used at LSU for EXAFS catalyst studies as well as modifying it for the *in situ* studies. Initial *in situ* studies will be carried out at 280°C and 1.8 atmospheres to emulate the studies carried out at Clemson University. The data should contain information about the phase transformations that occur during the Fischer-Tropsch synthesis.

During the period of Feb. 26 – Mar. 15, Mr. Andrew Campos who is a PhD student at LSU visited Clemson University almost entirely funded by the Louisiana Board of Regents to learn the SSITKA method and to participate in discussions about the catalyst preparation and reaction results. The visit was extremely beneficial allowing the two groups (CU and LSU) to strengthen their collaboration and exchange research ideas relevant to this project.

2.0 Conclusions

Characterization of catalysts containing a third transition metal by SEM and EDX showed that the all elements were well distributed throughout the catalyst. The catalyst particles were observed to be flat and irregular shaped with some uneven surfaces. Adding different transition metals to Fe-based FTS catalysts did not significantly impact the reducibility of the Fe. However, the activity of catalyst was affected by both Fe

reducibility and BET surface area. There is a combination of these 2 factors necessary in order to archive of catalysts with high activities.

Next Quarter's Activities

Research to be carried out at Clemson University in the next quarter will focus on FeZr catalysts. At the same time, catalysts promoted with K will be prepared and tested for CO hydrogenation.

During the next quarter at LSU, the Lytle Detector will be set up for EXAFS studies reactions during which will require setting up flow rates, pressure and temperature inside the detector itself. *In situ* tests are to begin in July-August. In the meantime, XRD will be carried out at LSU and used to determine the phases in the as-prepared samples. Fe K α excitation will be used as well as noise-free Si-based sample holders, both greatly reduce the noise that was found with the Rigaku Miniflex using Cu K α excitation.

(23) Energy Conservation Sciences for operation and Security of Large-Scale Systems

The objectives of the proposed effort are to expand and/or supplement the research presently underway as past of the Center on Security of Large Scale Systems. In particular, the project will seek to (1) expand solid-state research in the area of Silicon Carbide (SiC) for the purpose of reducing size, weight, and cost of power converters for motor drives and distributed generation, (2) to investigate methods of motor control including the advantages of SiC devices to increase the efficiency and reduce the cost of electric drives, and (3) to incorporate the results of the Center's research in fuel cell testing and modeling to suggest design and operation of these devices in distributed generation during islanding of an Electric power Grid.

Total project cost: \$322,834

Funding request: \$249,999

Project Lead: Purdue University

Project Participants: Wright State University

Start Date: May 23, 2005

End Date: May 23, 2007

Presentations/Publications

None.

Patents

None.

Progress in Past Quarter and Current Status

Task 1 Silicon Carbide Devices for Advanced, High-Efficiency Power Conversion

Michael Capano, Purdue University

Objectives:

The objectives of the SiC component of this research are to (1) develop criteria for the selection of SiC SBDs or PiN diodes and, (2) examine power dissipation and cooling requirements needed for SiC electronics.

Background:

To accomplish these objectives, simulation of SiC diodes are being performed using *Medici*, with the purpose of designing PiN and SBD diodes with nominally equivalent voltage ratings. Selection of PiN and SBDs are based on simulations using total power dissipation as the criterion for selection. Also, these simulations serve the purpose of defining device structures to be examined experimentally. Two voltage regimes are investigated: 1000 V and 5000 V. PiN diodes and Schottky diodes nominally in the 1000 V range are finished or nearly fabricated and their electrical and thermal characteristics are being evaluated. All activities performed under this project fall into one of the four categories below:

1. Design system requirements for SiC diodes, including selection of adequate coolant. SiC PiN and Schottky diodes with similar voltage ratings (1500 V and 5000 V).
2. Build SiC PiN and Schottky diodes. Measure diode characteristics under forward (on-state) and reverse (off-state) bias conditions.
3. Develop selection criteria for choosing PiN or SBDs based on current rating, switching frequency and power density limitations.
4. Investigate cooling requirements for SiC devices.

Research Progress:

The objective for this quarter was to test 1000 V Schottky barrier diodes, and compare experimental data with *Medici* simulations. Devices with dimensions from 100 μm diameter up to 2 mm x 2 mm have been tested, but the experimental data presented in this progress report is only taken from 100 μm diameter diodes. The reason for examining the small diodes is ease of comparison with *Medici* simulations. Figure 1 illustrates a comparison between the forward bias characteristics from experimentally measured (green) and simulated (red) data. These data correspond to 100 μm diameter Schottky barrier diodes. There is significant difference in the shape of the curves. First, and most obvious, the experimental curve shows significant curvature from the expected linear (resistive) behavior exhibited by the simulated curve. Subsequent simulations indicate increasing the resistance of the backside (ohmic) contact does add curvature to the simulated profile, but only when unrealistically large resistance values are used in simulations. Ohmic contacts, therefore, are not the explanation. Neither is resistance of the epilayer, as shown by the reasonable slope of the simulated profile. The slope corresponds to an epilayer doping of $6 \times 10^{15} \text{ cm}^{-3}$, which is what was measured experimentally.

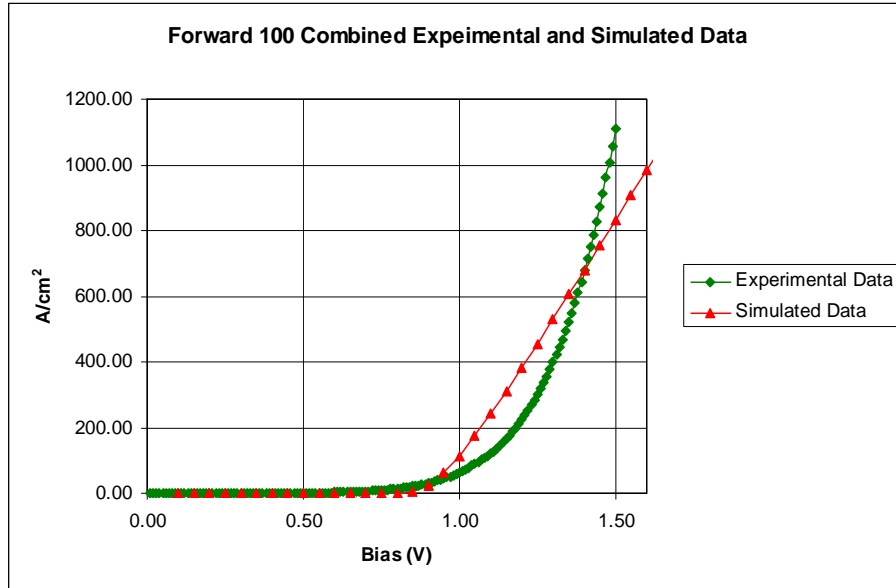


Fig. 1 Experimental and simulated forward bias characteristics for a 100 mm diameter Schottky barrier diode.

Work is continuing on improving the fit between experimental and simulated profiles.

PiN diode fabrication is in the final stages. At the time of this report, boron implantation of the resistive termination extension for the devices is being done. After receipt of the implanted samples, the implants will be annealed at 1050°C in argon for 90 min. This should be complete in the next week to 10 days.

Plans for Next Quarter:

Testing of 1000 V PiN diodes. Simulation of PiN diodes with 50 micron epilayers.

Task 2. Optimal Efficiency Motor Control Strategies

Marian Kazimierczuk, Wright State University

Objectives:

1.

The objective of this part of the project was to design a dc/ac variable- frequency three-phase power inverter, using Si and SiC power devices, estimate the inverter power losses and efficiency, and compare the losses and efficiency with Si and SiC devices.

Background:

The benefits of silicon carbide devices include high-breakdown voltage, high-temperature, high-frequency, high-reliability, and nearly zero reverse recovery. In previous quarters, electrical and thermal characteristics of SiC power devices were studied and areas of

applications were identified [1]. High-voltage SiC Schottky diodes appear to be the most promising SiC power devices for high-voltage, high-frequency applications, such as rectifiers and clamp circuits in dc/dc power converters and power-factor correctors [2]. The use of these diodes allows the designers to avoid snubber circuits and increase the switching frequencies. Also, parallel combinations of power SiC MOSFETs and SiC diodes are very promising arrangements in many applications. A topology of the dc/dc inverter was selected and designed. A Class D half-bridge dc/ac power inverter was selected for further investigations and the circuit was designed.

Publications:

A paper has been accepted for presentation: N. Das and M. K. Kazimierczuk, "Three-Phase Inverter with Silicon Carbide Diodes for Induction Motor Drives Used in Automobile Applications," 2007 Electrical Manufacturing Conference, Nashville, October 22-24, 2007.

Research Progress:

During this quarter, the behavior of silicon-carbide Schottky diodes was studied for applications in the ac/dc three-phase power conversion under the energy recovery operating conditions. Equations for the current and voltage waveforms were derived. The turn-off and turn-on transitions were extensively studied. Equation for conduction losses and switching losses were derived for silicon carbide diodes. The effect of the dead time on the switching losses was also investigated. The efficiency of the inverter was estimated. It was found that the dead time has a significant effect on the inverter efficiency. The analytical equations were validated by simulations of the inverter under various operating conditions.

Plans for Next Quarter:

The plans for the next quarter are to study the performance of the transistors in the three-phase inverter.

Task 3 Islanding and Distributed Generation for Enhanced Electric Power Grid Security

Academic Faculty:

Shripad Revankar, Associate Professor, Department of Nuclear Engineering, PU
Mitch Wolff, Professor, Department of Mechanical Engineering, WSU

Graduate Students:

Brian Wolf	M.S. Candidate Nuclear Engineering, PU
Karleine Justice	M.S. Candidate Mechanical Engineering, WSU
Carlos Gutierrez	M.S. Candidate Mechanical Engineering, WSU

Objective:

[1] N. Das and M. K. Kazimierczuk, "Applications of Silicon Carbide Power Devices in Power Electronics," Electrical Manufacturing and Coil Winding Association, Indianapolis, IN, September 18-20, 2006.

[2] D. Murthy and M. K. Kazimierczuk, "Active Clamp Circuits for Flyback PWM DC-DC Converter," Electrical Manufacturing and Coil Winding Association, Indianapolis, IN, September 18-20, 2006.

Investigate the control and performance of distributed generation during islanding of an electric power grid. High temperature fuel cell hybrid systems will be used for power generation.

Background:

Advancement in research of distributed generation of electrical power is a result of energy security issues and changing markets and technologies. Fuel cell hybrid technologies which integrate high temperature fuel cells with another power generation technology have promising abilities which make them an important research topic for development and commercialization. They meet many demands of U.S. energy goals of the future including independence from foreign sources, greater security, and pollution free emissions.

Previous work accomplished includes a thorough literature survey on hybrid fuel cell distributed generation systems. Steady state models for both Molten Carbonate Fuel Cells (MCFC) and Turbines of different capacities have been created. Other component models such as oxidizer, and heat exchangers have also been developed for steady state conditions. Certain controls were then implemented to begin the transition to dynamic modeling. Dynamic modeling of the fuel cell was successful and benchmarked with model results in literature. Multiple visits between Wright State and Purdue have proven to be very productive. Coupling of the MCFC fuel cell model and the turbine model has been a success. Fuel pre-conditioner models for the hybrid system are complete along with controls. Controls for the entire fuel cell hybrid system have been incorporated with control objectives met.

Research Progress:

Control objectives have been established and a control system has been implemented. PID type controllers are used to control stack temperature, oxidizer flow rate, and inlet fuel temperature and flow rate. The model has been studied on both steady state and dynamic levels. A few graphs of information for system layout, steady state and dynamic response of the system are shown below.

A Solid Oxide Fuel Cell model has been further developed. Specifically, an energy balance, and mass balances of the solid oxide fuel cell system have been produced and implemented into MATLAB/Simulink. Further developments of this system include performance calculations. Information on specific SOFC design variables has been gathered.

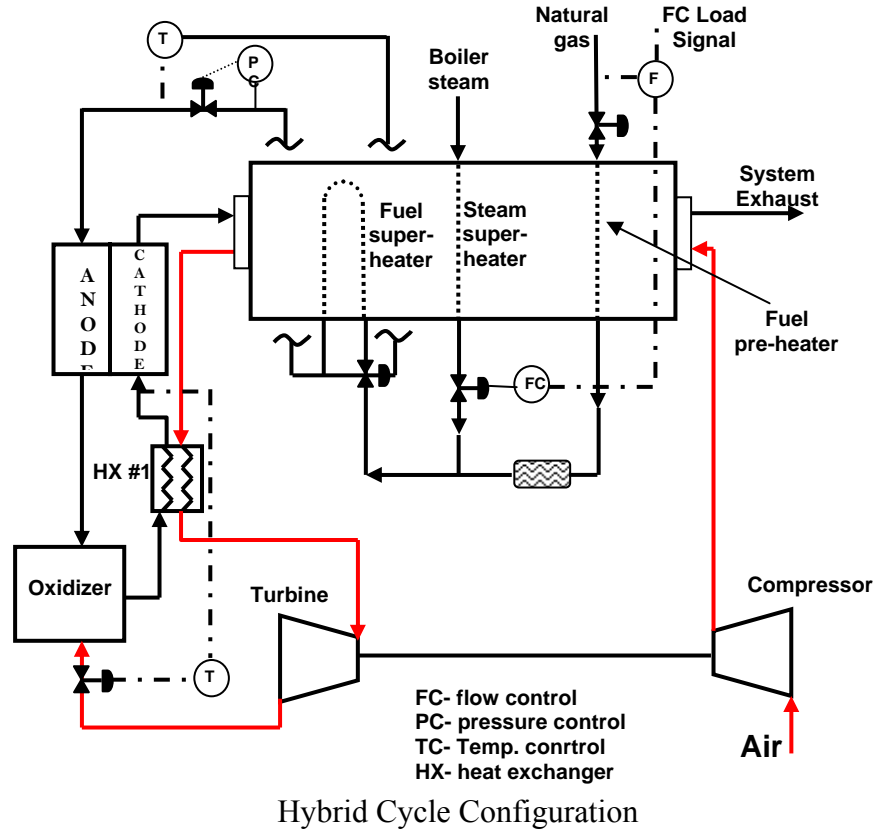


Fig. 2 Steady State Results of Hybrid System with constant current load density, fuel utilization and steam to carbon ratio.

FC Current Density (mA/cm²)	160
Fuel Utilization	0.75
Natural Gas Flow rate (mol/s)	30.43
Steam to Carbon Ratio	2
Oxidizer Air Flow (mol/s)	319.5
Number of Stacks	64
Cathode Inlet Temperature (K)	825.3
Anode Inlet Temperature (K)	861
Stack Temperature (K)	949
Cell Voltage (Volts)	0.67
Fuel Cell DC Power (MW)	8.47
Turbine Output Power (MW)	3.836
Total Plant Output (MW)	11.1
Overall LHV efficiency	59.70%

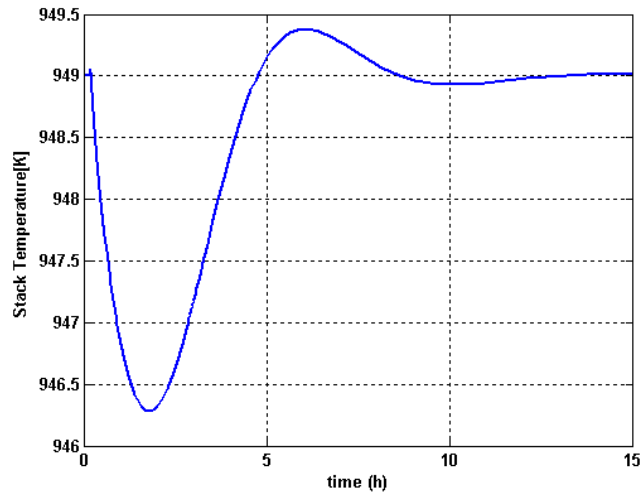
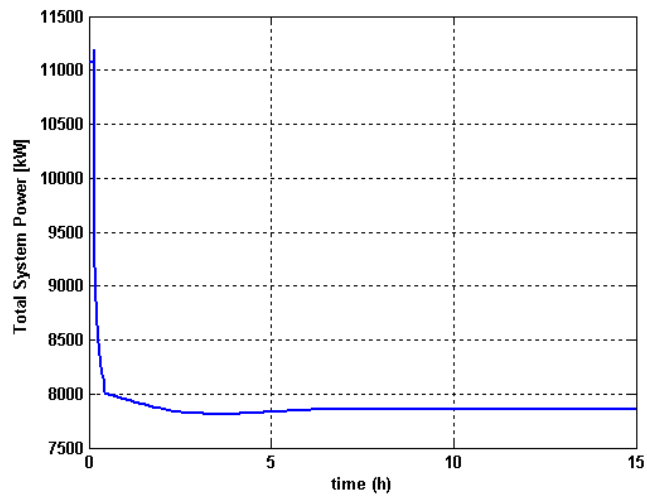


Fig. 3 Dynamic Response of FC Stack Temperature for hybrid system to 25% load reduction on fuel cell with a stack temperature control objective set point of 949 K.



Dynamic response of Total System Power for hybrid system with 25% load reduction on fuel cell.

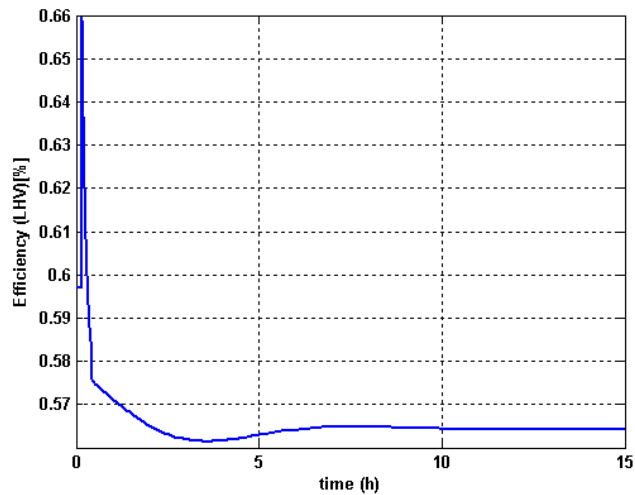


Fig. 4 Dynamic response of Hybrid system LHV efficiency for a 25 % load reduction on fuel cell.

Plans for Next Quarter:

After studying the performance of the fuel cell hybrid system, some future goals have been established.

1. Perform parametric studies to help optimize the system with respect to design variables such as fuel utilization, gas turbine power fraction, and oxidizer flow rates.
2. Create a reduced order model based on dynamic response assumptions. This would reduce the computational power required to solve long transients as well as minimize the ‘stiffness’ of the mathematical model.
3. Look further into different hybrid layouts.
4. Gather experimental data of ‘proof-of-concept’ test to further validate the model results.